STScI | SPACE TELESCOPE SCIENCE INSTITUTE

JWST TECHNICAL REPORT

Title: NIRISS Commissioning Results: NIS-019 NRM Performance (NGAS CAR-703, APT 1093)	Doc #: JWST-STScI-008334, SM-12 Date: 12 December 2022 Rev: -
Authors: Anand Sivaramakrishnan, Deepashri Thatte, Rachel Cooper, Thomas Vandal, Jens Kammerer, and the NIRISS Team Phone: 410-338-4888	Release Date: 14 March 2023

1 Abstract

We present the analysis and results of the commissioning activity NIS-019 NIRISS NRM Performance (NGAS CAR-703, APT 1093, PI Thatte). NIRISS NRM is the first ever space-based use of a non-redundant aperture mask (Sivaramakrishnan et al., 2023). NRM Performance met its Science Readiness Criterion of clear detection of a known binary star using the Non-Redundant Mask (NRM) pupil mask. The activity achieved its principal secondary goals: estimating the amount of Charge Migration (CM), as well as exercising Kernel Phase Interferometry (KPI) image analysis with the NRM's Aperture Masking Interferometry (AMI) (Kammerer et al. 2023) mode of the Astronomer's Proposal Tool (APT) template and the CLEARP element of the Pupil Wheel (PW).

2 Introduction

This activity acquired and analyzed science data on a typical AMI mode target using the NRM in the Pupil Wheel (PW) and three filters, F480M, F430M, F380M, in the Filter Wheel (FW) (see Figure 2-1). The multiple star system AB Dor and two calibrators were observed and analyzed. The AB Dor AC pair, treated as a binary, was used to demonstrate AMI science readiness. Four putative single stars were observed through the F480M in FW and CLEARP in the PW to demonstrate sufficiently deep contrast by using KPI analysis of these images.

Observations 1-11 (Epoch 1) commenced on May 23, 2022 at 02:27 ET (2022-05-23 06:26:46.331 UTC; L + 149 days) and had a total duration of about 9.3 hours. The observations were repeated (with slight modifications) to provide Observations 12-23 (Epoch 2) on Jun 5, 2022 at 09:28 ET (2022-06-05 13:28:44.649 UTC; L + 162 days) because Epoch 1 data did not meet AMI's science requirement on Target Acquisition (TA) placement accuracy. The target centroiding and placement issue responsible for the Epoch 1 data problem and its correction were tracked in JIRA issue JWSTOSS-7736.

Epoch 1, and separately, Epoch 2 observations were scheduled as non-interruptible in the APT's JWST Program 1093.

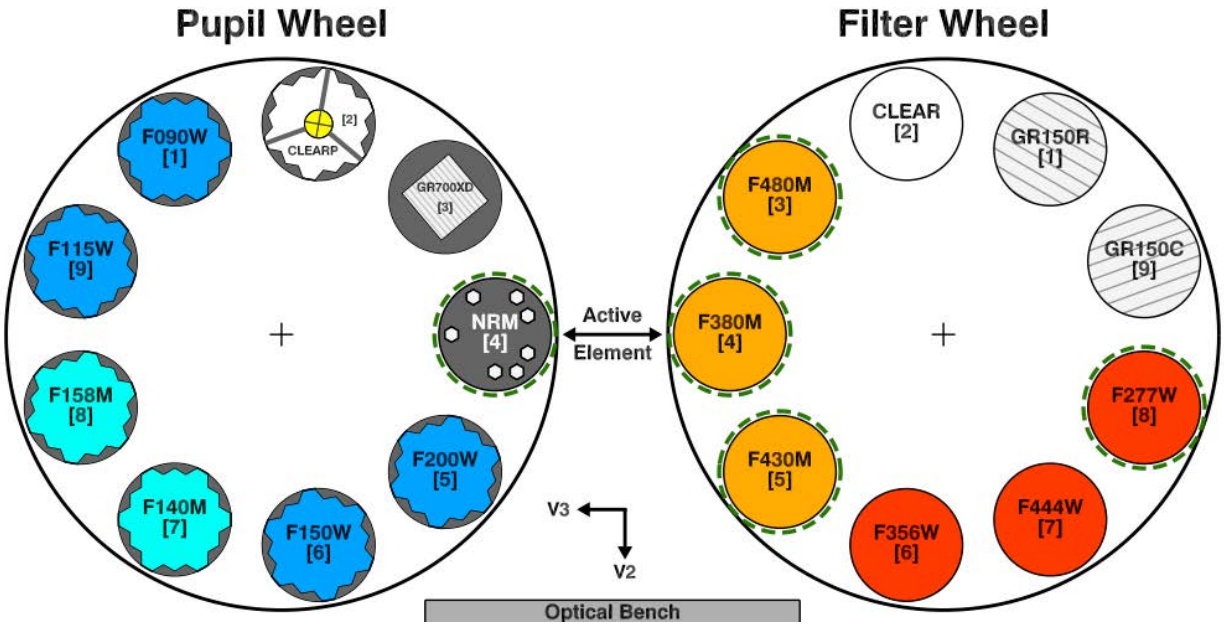

Figure 2-1. Schematic of the NIRISS Dual Wheel (DW). A photon traverses the Pupil Wheel (PW) before the Filter Wheel (FW). The wheel center to optical element center is 110 mm. The JWST pupil is nominally 40 mm diameter on these wheels, which are at or close to pupil. The NRM can be used with the four filters circled in green. Target acquisition is always performed using F480M, with brighter targets using the NRM, and fainter ones CLEARP.

3 Observations

When Fine Guide for a visit is achieved by JWST's Fine Guidance Sensor, the target is placed in the 64x64 SUBTAAMI subarray contiguous with the AMI 80x80 science SUB80 subarray After the target location is determined with a centroiding algorithm (Holfeltz et al., 2015), it is moved to one of four pre-defined positions, POS1, POS2, POS3, and POS4 in SUB80 (see NIRISS AMI Dithers in JDox pages).

Table 3-1 lists target information for the second set of observations. The first set of 11 observations did not meet Science Requirements–target placement to within 0.25 of a detector pixel from the commanded location. Although the TA centroiding algorithm worked as expected, the Small Angle Maneuver (SAM) failed to move the target to the designated position on the AMI science subarray (SUB80). Table 3-2 lists the exposures of the second set (Observations 12-23) after the On-Board Script Subsystem (OSS) software was corrected to command the appropriate target placement SAM. We note that even though target placement error exceeded its required limit, the first set of observations did meet the AMI Science Readiness Criterion of measuring AB Dor AC's binary parameters. While the first set of observations met the Science Readiness Criterion for NIS-019, its TA placement error would result in AMI data with unacceptably large sensitivity to flat fielding errors, and poorer achievable contrast. The rest of this report is restricted to the analysis of the second set of observations.

Table 3-1. Targets Summary

Name	RA (hms)	Dec (Deg)
AB Dor	05 28 44.9641	-65 26 52.74
HD-37093	05 31 8.2802	-65 07 41.99
HD-36805	05 29 6.4686	-66 41 13.00
J062802.01-663738.0	06 28 2.0285	-66 37 37.99
TYC-8906-1660-1	06 27 0.5419	-66 21 58.87
CPD-66-562	06 31 36.6320	-66 21 47.59
CPD-67-607	06 29 31.9214	-67 13 12.91

Table 3-2 contains parameters pertaining to each uncalibrated data file prior to processing through the JWST data pipeline. Version 1.5.1 of the JWST pipeline was used to obtain calibrated data during commissioning. The first four entries in each observation are SUBTAAMI data used for target acquisition. Columns in the table are:

PW – Active element in the Pupil Wheel

- FW – Active element in the Filter Wheel
- NINTS – Number of integrations
- NGROUPS – Number of groups in an integration (“INT”)
- Level1b – Uncalibrated 4-dimensional data file name root

Table 3-2. Observations 12-23 in Program

PW	FW	NINTS	NGROUPS	Level1b
Obs 12 AB DOR Pri 1				
NRM	F480M	1	7	jw01093012001_02101_00001_nis_uncal
NRM	F480M	1	7	jw01093012001_02101_00002_nis_uncal
NRM	F480M	1	7	jw01093012001_02101_00003_nis_uncal
NRM	F480M	1	7	jw01093012001_02101_00004_nis_uncal
NRM	F480M	69	5	jw01093012001_03102_00001_nis_uncal
NRM	F430M	82	4	jw01093012001_03103_00001_nis_uncal
NRM	F380M	160	2	jw01093012001_03104_00001_nis_uncal
NRM	F480M	29	13	jw01093012001_03105_00001_nis_uncal
Obs 13 AB DOR Pri 1 + offset				
NRM	F480M	1	7	jw01093013001_02101_00001_nis_uncal
NRM	F480M	1	7	jw01093013001_02101_00002_nis_uncal
NRM	F480M	1	7	jw01093013001_02101_00003_nis_uncal
NRM	F480M	1	7	jw01093013001_02101_00004_nis_uncal
NRM	F480M	69	5	jw01093013001_03102_00001_nis_uncal
NRM	F430M	82	4	jw01093013001_03103_00001_nis_uncal
NRM	F380M	160	2	jw01093013001_03104_00001_nis_uncal
NRM	F480M	29	13	jw01093013001_03105_00001_nis_uncal
Obs 14 AB DOR Pri 1, 5 Sub.				
NRM	F480M	1	7	jw01093014001_02101_00001_nis_uncal

PW	FW	NINTS	NGROUPS	Level1b
NRM	F480M	1	7	jw01093014001_02101_00002_nis_uncal
NRM	F480M	1	7	jw01093014001_02101_00003_nis_uncal
NRM	F480M	1	7	jw01093014001_02101_00004_nis_uncal
NRM	F480M	69	5	jw01093014001_03102_00001_nis_uncal
NRM	F480M	69	5	jw01093014001_03102_00002_nis_uncal
NRM	F480M	69	5	jw01093014001_03102_00003_nis_uncal
NRM	F480M	69	5	jw01093014001_03102_00004_nis_uncal
NRM	F480M	69	5	jw01093014001_03102_00005_nis_uncal
Obs 15 Calibrator HD-37093 Pri 1				
NRM	F480M	1	11	jw01093015001_02101_00001_nis_uncal
NRM	F480M	1	11	jw01093015001_02101_00002_nis_uncal
NRM	F480M	1	11	jw01093015001_02101_00003_nis_uncal
NRM	F480M	1	11	jw01093015001_02101_00004_nis_uncal
NRM	F480M	61	12	jw01093015001_03102_00001_nis_uncal
NRM	F430M	78	9	jw01093015001_03103_00001_nis_uncal
NRM	F380M	118	4	jw01093015001_03104_00001_nis_uncal
Obs 16 Calibrator HD-37093 Pri 1 + offset				
NRM	F480M	1	11	jw01093016001_02101_00001_nis_uncal
NRM	F480M	1	11	jw01093016001_02101_00002_nis_uncal
NRM	F480M	1	11	jw01093016001_02101_00003_nis_uncal
NRM	F480M	1	11	jw01093016001_02101_00004_nis_uncal
NRM	F480M	61	12	jw01093016001_03102_00001_nis_uncal
NRM	F430M	78	9	jw01093016001_03103_00001_nis_uncal
NRM	F380M	118	4	jw01093016001_03104_00001_nis_uncal
Obs 17 Calibrator HD-37093 Pri 1, 5-pt SD				
NRM	F480M	1	11	jw01093017001_02101_00001_nis_uncal
NRM	F480M	1	11	jw01093017001_02101_00002_nis_uncal
NRM	F480M	1	11	jw01093017001_02101_00003_nis_uncal
NRM	F480M	1	11	jw01093017001_02101_00004_nis_uncal
NRM	F480M	61	12	jw01093017001_03102_00001_nis_uncal
NRM	F480M	61	12	jw01093017001_03102_00002_nis_uncal
NRM	F480M	61	12	jw01093017001_03102_00003_nis_uncal
NRM	F480M	61	12	jw01093017001_03102_00004_nis_uncal
NRM	F480M	61	12	jw01093017001_03102_00005_nis_uncal
Obs 18 HD-36805 Pri 1				
NRM	F480M	1	7	jw01093018001_02101_00001_nis_uncal
NRM	F480M	1	7	jw01093018001_02101_00002_nis_uncal
NRM	F480M	1	7	jw01093018001_02101_00003_nis_uncal
NRM	F480M	1	7	jw01093018001_02101_00004_nis_uncal
NRM	F480M	65	9	jw01093018001_03102_00001_nis_uncal

PW	FW	NINTS	NGROUPS	Level1b
NRM	F430M	82	6	jw01093018001_03103_00001_nis_uncal
NRM	F380M	122	3	jw01093018001_03104_00001_nis_uncal
Obs 19 HD-36805 Pri 1 + offset				
NRM	F480M	1	7	jw01093019001_02101_00001_nis_uncal
NRM	F480M	1	7	jw01093019001_02101_00002_nis_uncal
NRM	F480M	1	7	jw01093019001_02101_00003_nis_uncal
NRM	F480M	1	7	jw01093019001_02101_00004_nis_uncal
NRM	F480M	65	9	jw01093019001_03102_00001_nis_uncal
NRM	F430M	82	6	jw01093019001_03103_00001_nis_uncal
NRM	F380M	122	3	jw01093019001_03104_00001_nis_uncal
Obs 20 HD-36805 Pri 1, 25 SD				
NRM	F480M	1	7	jw01093020001_02101_00001_nis_uncal
NRM	F480M	1	7	jw01093020001_02101_00002_nis_uncal
NRM	F480M	1	7	jw01093020001_02101_00003_nis_uncal
NRM	F480M	1	7	jw01093020001_02101_00004_nis_uncal
NRM	F480M	65	9	jw01093020001_03102_00001_nis_uncal
NRM	F480M	65	9	jw01093020001_03102_00002_nis_uncal
NRM	F480M	65	9	jw01093020001_03102_00003_nis_uncal
NRM	F480M	65	9	jw01093020001_03102_00004_nis_uncal
NRM	F480M	65	9	jw01093020001_03102_00005_nis_uncal
NRM	F480M	65	9	jw01093020001_03102_00006_nis_uncal
NRM	F480M	65	9	jw01093020001_03102_00007_nis_uncal
NRM	F480M	65	9	jw01093020001_03102_00008_nis_uncal
NRM	F480M	65	9	jw01093020001_03102_00009_nis_uncal
NRM	F480M	65	9	jw01093020001_03102_00010_nis_uncal
NRM	F480M	65	9	jw01093020001_03102_00011_nis_uncal
NRM	F480M	65	9	jw01093020001_03102_00012_nis_uncal
NRM	F480M	65	9	jw01093020001_03102_00013_nis_uncal
NRM	F480M	65	9	jw01093020001_03102_00014_nis_uncal
NRM	F480M	65	9	jw01093020001_03102_00015_nis_uncal
NRM	F480M	65	9	jw01093020001_03102_00016_nis_uncal
NRM	F480M	65	9	jw01093020001_03102_00017_nis_uncal
NRM	F480M	65	9	jw01093020001_03102_00018_nis_uncal
NRM	F480M	65	9	jw01093020001_03102_00019_nis_uncal
NRM	F480M	65	9	jw01093020001_03102_00020_nis_uncal
NRM	F480M	65	9	jw01093020001_03102_00021_nis_uncal
NRM	F480M	65	9	jw01093020001_03102_00022_nis_uncal
NRM	F480M	65	9	jw01093020001_03102_00023_nis_uncal
NRM	F480M	65	9	jw01093020001_03102_00024_nis_uncal
NRM	F480M	65	9	jw01093020001_03102_00025_nis_uncal

PW	FW	NINTS	NGROUPS	Level1b
Obs 21 J062802.01-663738.0				
NRM	F480M	1	19	jw01093021001_02101_00001_nis_uncal
NRM	F480M	1	19	jw01093021001_02101_00002_nis_uncal
NRM	F480M	1	19	jw01093021001_02101_00003_nis_uncal
NRM	F480M	1	19	jw01093021001_02101_00004_nis_uncal
NRM	F480M	10	10	jw01093021001_03102_00001_nis_uncal
CLEARP	F480M	239	14	jw01093021001_03103_00001_nis_uncal
CLEARP	F480M	239	14	jw01093021001_03103_00002_nis_uncal
Obs 22 TYC-8906-1660-1				
NRM	F480M	1	19	jw01093022001_02101_00001_nis_uncal
NRM	F480M	1	19	jw01093022001_02101_00002_nis_uncal
NRM	F480M	1	19	jw01093022001_02101_00003_nis_uncal
NRM	F480M	1	19	jw01093022001_02101_00004_nis_uncal
NRM	F480M	10	10	jw01093022001_03102_00001_nis_uncal
CLEARP	F480M	236	13	jw01093022001_03103_00001_nis_uncal
CLEARP	F480M	236	13	jw01093022001_03103_00002_nis_uncal
Obs 23 CPD-67-607				
NRM	F480M	1	19	jw01093023001_02101_00001_nis_uncal
NRM	F480M	1	19	jw01093023001_02101_00002_nis_uncal
NRM	F480M	1	19	jw01093023001_02101_00003_nis_uncal
NRM	F480M	1	19	jw01093023001_02101_00004_nis_uncal
NRM	F480M	10	10	jw01093023001_03102_00001_nis_uncal
CLEARP	F480M	232	13	jw01093023001_03103_00001_nis_uncal
CLEARP	F480M	232	13	jw01093023001_03103_00002_nis_uncal

4 Analysis Steps

4.1 Data Processing

AMI data were collected at the PRIMARY dither position (“pri1”) and the PRIMARY position with a constant added OFFSET (“pri2”) during Epoch 2. Prior to data reduction and analysis, standard data verification checks were performed. We confirmed that the correct number of uncal.fits files were available and downloaded from the Mikulski Archive for Space Telescopes (MAST). The following FITS header keywords of each file were checked for basic correctness: PWCPOS, FWCPOS, TFRAME, TGROUP, EFFEXPTM, DURATION, NINTS, NGROUPS, V2_REF, V3_REF, SUBSTRT1, SUBSTRT2, SUBSIZE1, SUBSIZE2. Dither keywords PATTTYPE, PATT_NUM, PATTSIZE, NUMDTHPT, XOFFSET, YOFFSET were printed and checked manually. The only incorrect header keywords found were DURATION and EFFEXPTM, which differed very slightly from the expected values due to the small number of significant figures used in the onboard calculation (documented in JIRA issue JWSTOSS-7663).

Program-specific validation matched each exposure file to one listed in the program APT file. Cross-matched values are observation number, number of groups, number of integrations, pupil, filter, and primary and subpixel dither pattern. All exposures were present and correct in observations taken at both epochs.

While level 1a, 2a, and 2b pipeline products were available in the Mikulski Archive for Space Telescopes (MAST), the image cube calints.fits products were not, so we reprocessed the exposures through the Detector1 and Image2 pipelines using the latest in-flight reference files. We skipped the IPC step in Detector1 and the photom and resampled steps in Image2. We also saved calibrated 4-dimensional ramp products for additional data checks. Two example calibrated (cal.fits) images of AB Dor in F480M are shown in Figure 4-1.

Bad pixels are flagged by the pipeline in the DQ array of each data file, but simply masking these pixels is insufficient for AMI; the bad pixels need to be corrected in the data in order to accurately centroid the image for image-plane observable extraction. We used a stand-alone code that uses the pupil geometry to identify noise in the image and correct pixel values that have unphysical signal. Such pixels place power in the image's Fourier transform where there should be no signal, which makes them identifiable. The method we utilized is described in Ireland (2013) and refined in Kammerer et al. (2019). A version of this code developed specifically for AMI was used to apply this correction to the calints files before extraction of interferometric observables.

Pipeline-calibrated and bad-pixel corrected calints FITS files can be input to either the STScI-supported ImPlaneIA or Sydney University's AMICAL packages that extract interferometric observables from image plane data. These observables are a fringe amplitude in degrees, and a fringe visibility–a dimensionless number between 0 and 1– for each baseline between the seven holes in the NRM. A total target flux and a constant "bias" or pedestal in the image is also measured, though the latter do not play a role in interferometric analyses. Both packages produce standardized OIFITS v2 format FITS files that are widely used in optical and IR interferometry. The target's observables are calibrated using the calibrator star's observables, and calibrated OIFITS files are analyzed by either CANDID or Fouriever binary star parameter extraction codes to extract binary parameters: contrast in magnitudes (dM), Separation (Sep), and Position Angle (PA).

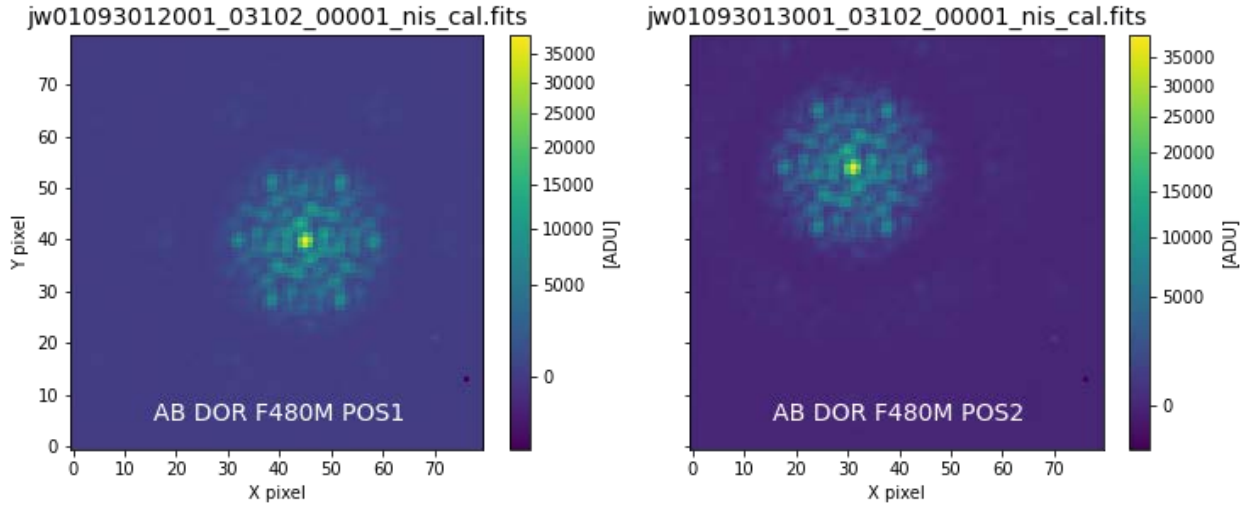

Figure 4-1: Pipeline-calibrated exposures of commissioning target AB Dor in F480M at two primary dithers. AMI mode calibrated data is in ADU rather than MJy/sr, which is atypical of most other JWST science data.

The analysis steps described in the following subsections are:

1. Science readiness criterion
2. Compare observables to simulations and analytical estimates
3. Calibrated single star CPs are close to zero, SqVs close to unity
4. Average CPs of calibrators are close to zero, SqVs close to unity
5. Data quality check
6. Subaperture positions check
7. PSF location check
8. Dithers and subdithers location check
9. Charge migration existence
10. Kernel phase interferometry testing

4.2 NAP step 0: Science Readiness Criterion

AMI is required to reach binary point source contrast of 9-10 magnitudes at separations of 100-400mas. However, since NIRISS has no control of where the re-imaged JWST Primary Mirror is located in the instrument's entrance pupil, a lower contrast was used to define AMI Science Readiness. In order to account for possible early pupil alignment issues, AB Dor, a known multiple star system within JWST's Southern Continuous Viewing Zone, was chosen to demonstrate the steps involved in measuring the flux ratio, separation, and position angle of a binary. AB Doradus is a quadruple star system composed of two binaries separated by about 9": AB Dor A/C and AB Dor Ba/Bb. AB Dor A/C are, respectively, a pre-main-sequence K0V star (M_K = 4.686) and an ~M6 dwarf with ~50:1 contrast in the near-infrared. The expected separation, position angle, and contrast of the binary on the observation date are given in the first row of Table 4-3 (Sahlmann 2017 and references therein). This process exercised all the required steps for a higher contrast observation while allowing for unexpected but correctable problems to be identified. However, no such problems were encountered; the Science Readiness Criterion was easily met even without Target Acquisition meeting its Science Requirements by the analysis of both epochs' data.

The multiple star system AB Dor's calibrated fringe observables yielded binary parameters (contrast dM, separation SEP, and position angle PA) that agree with previously known (or extrapolated) values to within 3σ of the prior ground-based estimates in each of F380M, F430M, F480M.

Table 4-1 contains measured AB Dor AC binary point source parameters for all observations of the target AB Dor calibrated by calibrator observations made at the same location on the detector as the target. Two positions, the PRIMARY dither ("pri1") and the PRIMARY position with the offset ("pri2") are tested in Epoch 2. Calibrated OIFITS file names indicate the observation numbers of target and calibrator. (Table 3-2 notes which dither position was used for each observation). An 8-standard deviation detection is the largest significance that the software can report, rather than the actual detection confidence.

Table 4-1. Binary parameters extracted from AMI data measured by CANDID

CALIBRATED OIFITS FILE	SEP/mas	PA/deg	dM/mag	chi^2	nσ
obs012_pri1_sub0_calib_obs015_pri1_sub0_F480M	328.179 +/- 7.90	279.908 +/- 1.30	4.440 +/- 0.11	0.06	8.03
obs013_pri1_sub0_calib_obs016_pri1_sub0_F480M	330.894 +/- 8.61	279.405 +/- 1.35	4.485 +/- 0.11	0.07	8.03

CALIBRATED OIFITS FILE	SEP/mas	PA/deg	dM/mag	chi^2	nσ
obs012_pri1_sub0_calib_obs015_pri1_sub0_F430M	326.811 +/- 8.51	280.100 +/- 1.42	4.415 +/- 0.12	0.09	8.03
obs013_pri1_sub0_calib_obs016_pri1_sub0_F430M	326.536 +/- 8.78	279.367 +/- 1.44	4.474 +/- 0.11	0.09	8.03
obs012_pri1_sub0_calib_obs015_pri1_sub0_F380M	322.812 +/- 10.15	279.600 +/- 1.78	4.415 +/- 0.15	0.09	8.03
obs013_pri1_sub0_calib_obs016_pri1_sub0_F380M	393.508 +/- 9.49	425.517 +/- 1.39	4.353 +/- 0.15	0.09	8.03
obs012_pri1_sub0_calib_obs018_pri1_sub0_F480M	328.198 +/- 7.78	280.238 +/- 1.28	4.507 +/- 0.11	0.06	8.03
obs013_pri1_sub0_calib_obs019_pri1_sub0_F480M	328.870 +/- 8.45	279.935 +/- 1.36	4.554 +/- 0.11	0.06	8.03
obs012_pri1_sub0_calib_obs018_pri1_sub0_F430M	328.412 +/- 10.59	280.015 +/- 1.73	4.512 +/- 0.14	0.12	8.03
obs013_pri1_sub0_calib_obs019_pri1_sub0_F430M	327.088 +/- 8.21	279.662 +/- 1.32	4.529 +/- 0.11	0.07	8.03
obs012_pri1_sub0_calib_obs018_pri1_sub0_F380M	324.216 +/- 8.93	279.656 +/- 1.57	4.438 +/- 0.14	0.07	8.03
obs013_pri1_sub0_calib_obs019_pri1_sub0_F380M	328.393 +/- 9.95	280.448 +/- 1.73	4.417 +/- 0.15	0.09	8.03

Table 4-2 shows the Science Readiness Criteria pass/fail results for each filter, and target and calibrator placed at the same detector location, using CANDID binary star extraction software. All but one of the AB Dor observations detected AB Dor C within the required accuracy. One F380M observation detected a Fourier-aliased companion very far from the actual companion location. The aliasing occurs when companions reach the outer areas of the NRM field of view (the width of a single subaperture PSF's core, also called the Primary Beam). With a grey model this alias detection is suppressed, since the other two filters have wider fields of view because of their longer wavelengths.

Table 4-2. Science Readiness Pass/Fail per filter and target-calibrator pair (CANDID) within 3-σ of ground-based measurements.

Calibrated OIFITs	Sep	PA	DM
obs012_pri1_sub0_calib_obs015_pri1_sub0_F480M	True	True	True
obs013_pri1_sub0_calib_obs016_pri1_sub0_F480M	True	True	True
obs012_pri1_sub0_calib_obs015_pri1_sub0_F430M	True	True	True
obs013_pri1_sub0_calib_obs016_pri1_sub0_F430M	True	True	True
obs012_pri1_sub0_calib_obs015_pri1_sub0_F380M	True	True	True
obs013_pri1_sub0_calib_obs016_pri1_sub0_F380M	True	False	True
obs012_pri1_sub0_calib_obs018_pri1_sub0_F480M	True	True	True
obs013_pri1_sub0_calib_obs019_pri1_sub0_F480M	True	True	True
obs012_pri1_sub0_calib_obs018_pri1_sub0_F430M	True	True	True
obs013_pri1_sub0_calib_obs019_pri1_sub0_F430M	True	True	True
obs012_pri1_sub0_calib_obs018_pri1_sub0_F380M	True	True	True
obs013_pri1_sub0_calib_obs019_pri1_sub0_F380M	True	True	True

Table 4-3 shows the Science Readiness Criteria pass/fail results using all filters and a grey model for the binary star. Combined interferometric data taken through all three filters was analyzed with CANDID as well as the Fouriever code. The predicted values and uncertainties for position angle and separation on the observation date were derived using Hipparcos (HIP2) astrometry with model-independent masses for the components (Sahlmann 2017, code adapted by Kevin Volk). Approximate contrast in the three AMI filters was computed from Phoenix stellar models normalized for NIRISS AMI filters by Kevin Volk.

Table 4-3. Science Readiness Pass/Fail using all data and grey model using CANDID or Fouriever

	Sep/mas	PA/deg	dM/mag
Predicted	370.984 +/- 45.00	286.975 +/- 60.00	4.203 +/- 1.03
CANDID	327.292 +/- 2.63	279.901 +/- 0.44	4.469 +/- 0.04
Fouriever	326.850 +/- 2.45	279.899 +/- 0.43	4.460 +/- 0.04
CANDID pass	True	True	True
Fouriever pass	True	True	True

4.3 NAP step 1: Compare Observables to Simulations and Analytical Estimates

We required that measured closure phases (CPs) and Square Visibilities (SqVs) were comparable with CP and SqV derived from noiseless simulations of AB Dor, and with monochromatic analytical formulae for these parameters. We also verified that statistics of other fringe parameters looked reasonable, and statistics from pistons from all exposures confirmed primary mirror stability during each and across all observations.

AB Dor exposures were divided into 10 equal bins of averaged rate images. Each uncalibrated closure phase standard deviation (in sample space of 10) must be less than 0.1 radians (5.7 degrees), fringe amplitude standard deviations < 0.1. Bounds based on simulated commissioning data were relaxed given that these are the first space-based NRM observations. F480M pupil phases standard deviation should be < 50 nm OPD. Pupil rotation stability was not specified by the time data was acquired, but was measured in Section 4.8.

Each calibrator's data was also divided into 10 equal bins of averaged rate images. Each uncalibrated closure phase standard deviation (in sample space of 10) must be less than 0.1 radians, fringe amplitude standard deviations must be < 0.1. F480M pupil phases standard deviation should be < 50 nm OPD.

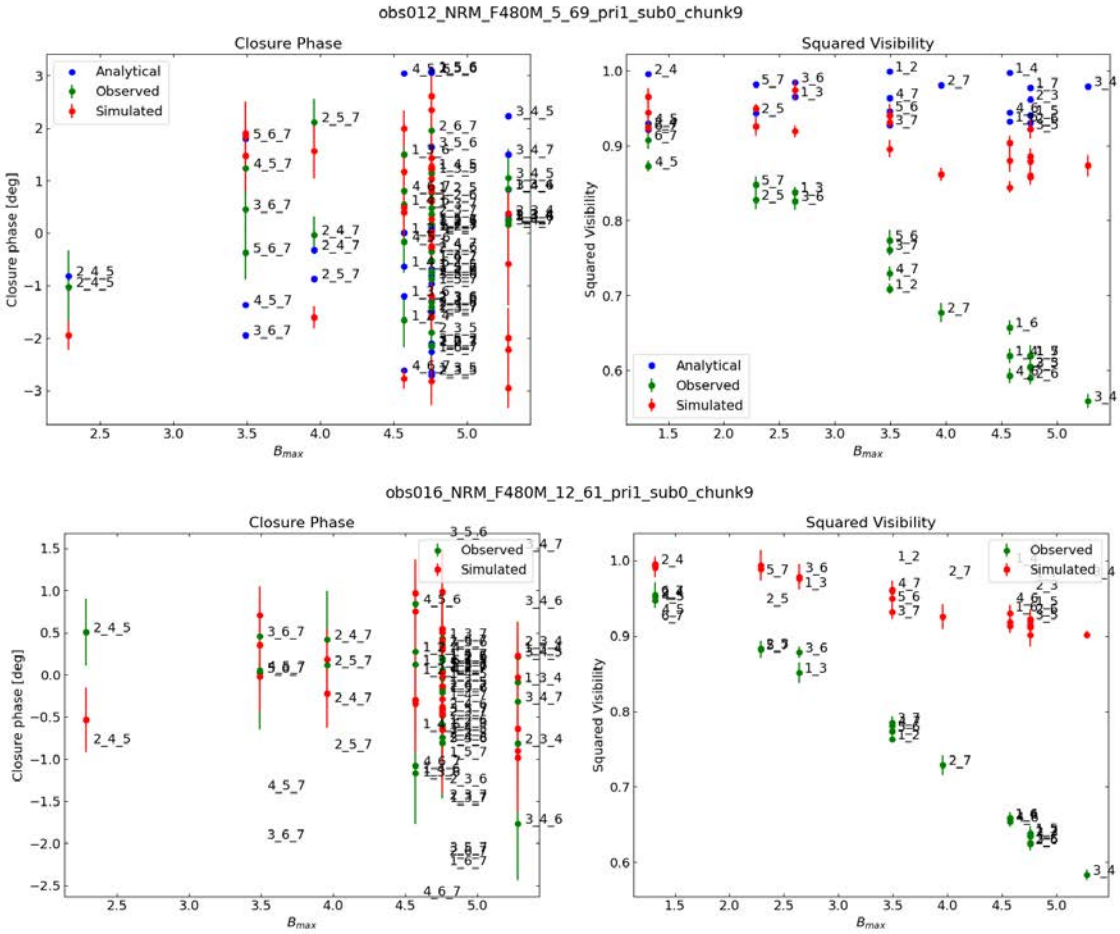

Figure 4-2. Observed raw closure phase standard deviations (green bars) lie well below the specified limit of 0.1 radians (5.7 degrees), and squared visibility standard deviations below 0.1. All measurements showed scatter similar to the one shown here. The top panels are for AB Dor AC, the bottom for one of the calibrator stars.

Differences in the sets of (the 7 zero mean) F480M pupil phases between all pairs of calibrators should have standard deviations < 50nm OPD (based on the requirement that wavefront correction not exceed 50 nm).

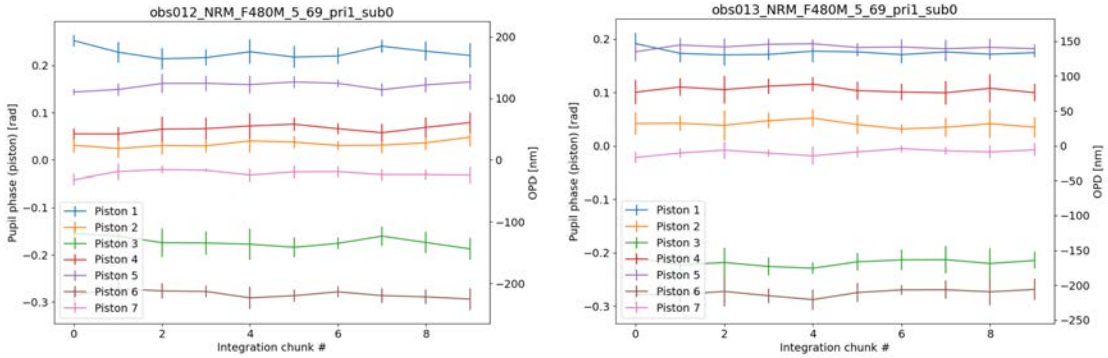

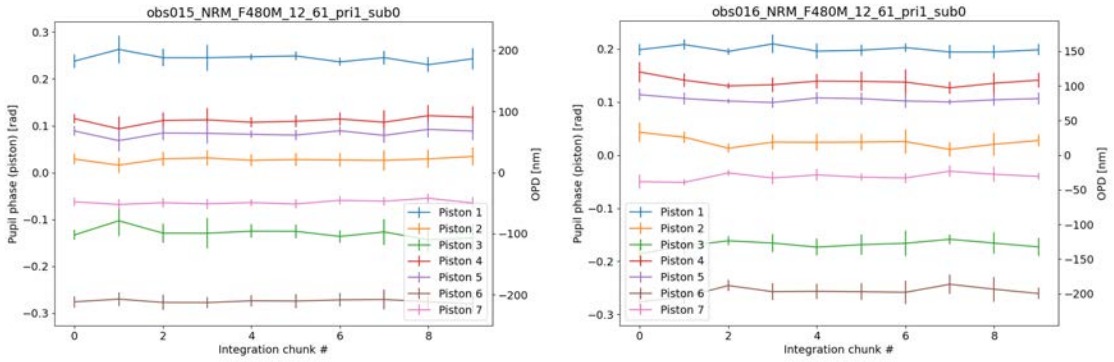

Figure 4-3. Seven segment pistons measured in target (top row) exposures and single star calibrators (bottom row) exposures displayed individual measurement standard deviations of ~15 nm. Integrations were split into ten equal-length sets (chunks), to monitor piston stability. Each observation was about 40 s, and piston measurement cadence was ~4 s. These measurements satisfy the requirement that piston standard deviations be below 50 nm.

We find that the standard deviations of the raw closure phases and squared visibilities in 10 bins meet the requirements of being below 0.1 radians for CPs, 0.1 for SqVs for both target and calibrator, as shown in Figure 4-2. Figure 4-3 demonstrates the piston stability during an exposure measured for AB Dor and one calibrator at two positions. The standard deviation of individual pistons is below the required 50 nm OPD, as is the standard deviation of one calibrator's pistons calibrated by the other.

4.4 NAP step 2: Calibrated single star CPs are close to zero and SqVs close to unity.

Calibrating one calibrator by the other produced zero-mean CPs, with a standard deviation of 1 to 2 degrees (0.015-0.035 radians), and SqVs within 0.005 of unity with standard deviations of 0.01-0.015. The requirement set for CP standard deviations was set from the heuristic of achievable flux ratio being the square root of the closure phase standard deviation (in radians). The standard deviation of all closure phases for a particular calibrated observation is of the order of 0.15 degrees (0.003 radian), which is expected to provide an achievable contrast of approximately 300:1. Calibrated squared visibilities of a single calibrated observation displayed a standard deviation of 0.003, as shown in Figure 4-4.

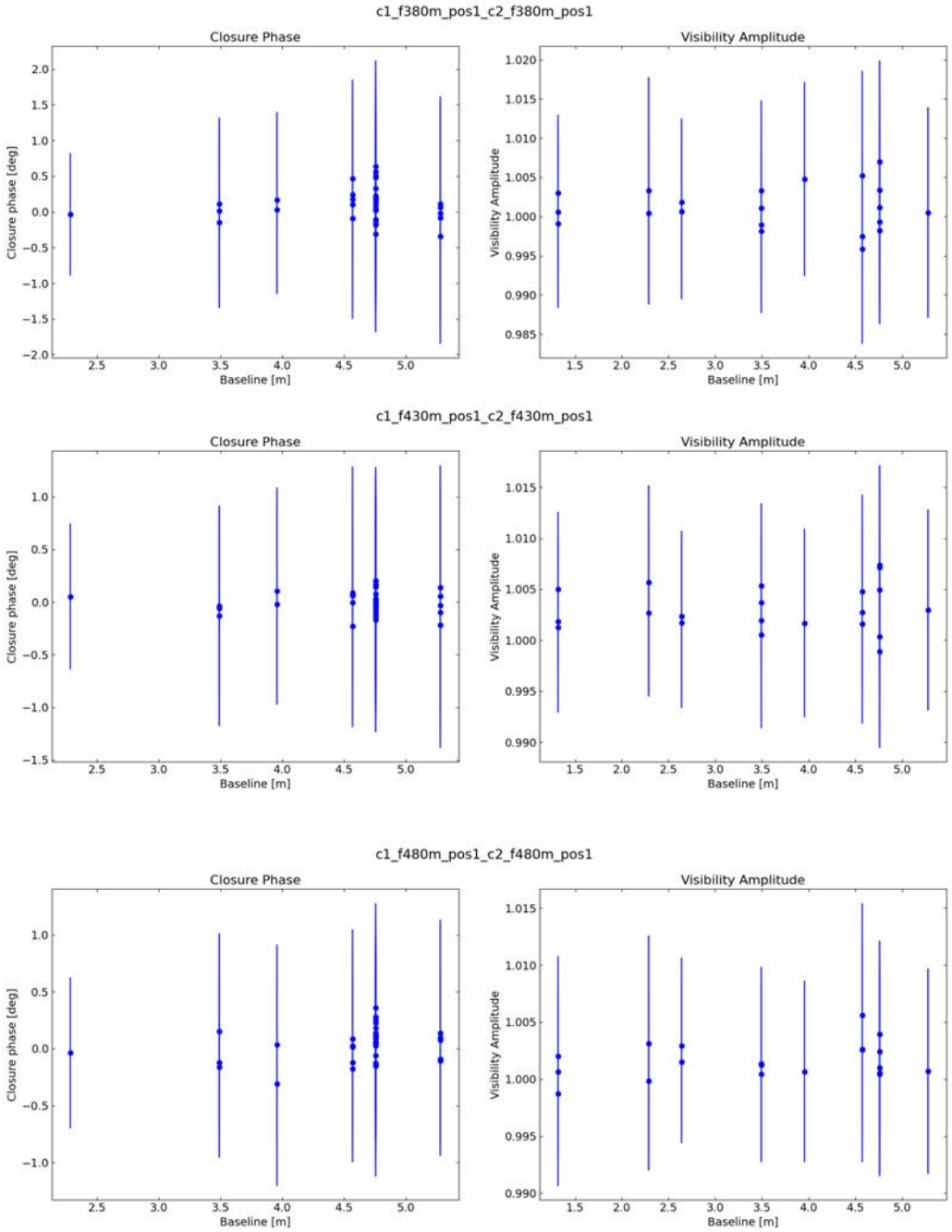

Figure 4-4. CPs and SqVs for one calibrator calibrated against the other. Data points cluster around their expected theoretical values of 0 for CPs and 1 for SqVs more tightly than their formal standard deviations might indicate they should.

4.5 NAP step 3: Average CPs of calibrators are close to 0 and SqVs close to unity.

We found that raw CPs of calibrator stars lay between 2 degrees of 0. Square visibilities did not reproduce simulated raw SqVs within 5-σ. SqVs were, however, repeatable at the same level as those extracted from noisy simulations. The reason for the observed SqVs decreasing with baseline length faster than those extracted from noisy simulations is not currently understood,

although this behavior is repeatable enough to be calibrated out of target observations by a calibrator PSF observation. Raw observables from one representative calibrator exposure are plotted in Figure 4-5.

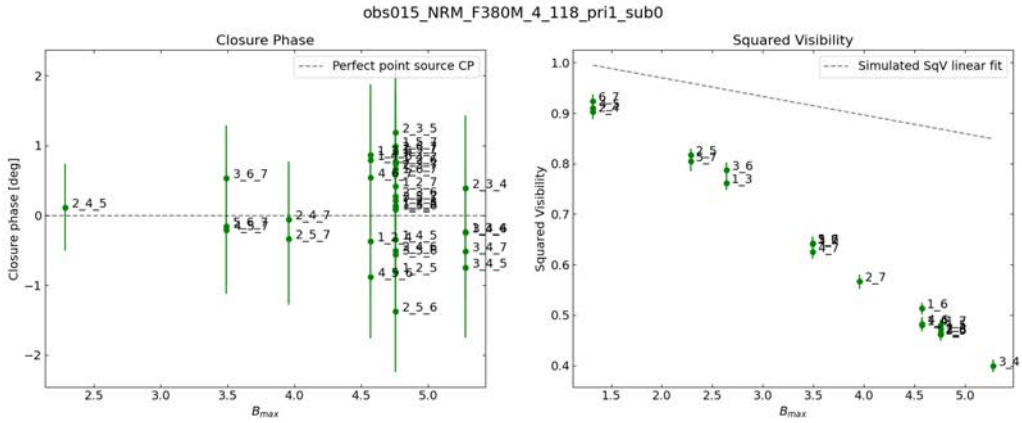

Figure 4-5. Raw CPs lie within 2 degrees of zero, raw SqVs are consistently below those of simulated data, although the scatter in their measurements is well below 0.1. This figure is representative of all calibrator data.

4.6 NAP step 4: Data quality is good, and there are no problems with observing conditions.

1. Check that DC levels–constant backgrounds in the images–measured by ImPlaneIA are consistent with measured detector read noise and drift given the binning of data into subsets of 10. Check that DC levels from bins of 10 integrations of pipeline-calibrated data are within 10σ of 0. Flux levels should be consistent with estimated photon noise and targets' brightnesses. Each of these requirements was satisfied. Figure 4-6 shows the mean background signal in a 5x5 region of the detector away from the PSF core as measured in simulated and observed data.
2. The requirement that the number of known 'DO_NOT_USE' (DNU) pixels flagged by the pipeline, as well as bad pixels identified by Kammerer-Ireland bad pixel fix in the cutout region used for fringe fitting do not exceed twice the number of DNU pixels in that region was satisfied. The Kammerer-Ireland algorithm identified of the order of 10 or fewer new bad pixels in each integration, whereas the number of DNU-flagged pixels in the cutout regions around pri1and pri2 respectively are of the order of 100 and 60 respectively.

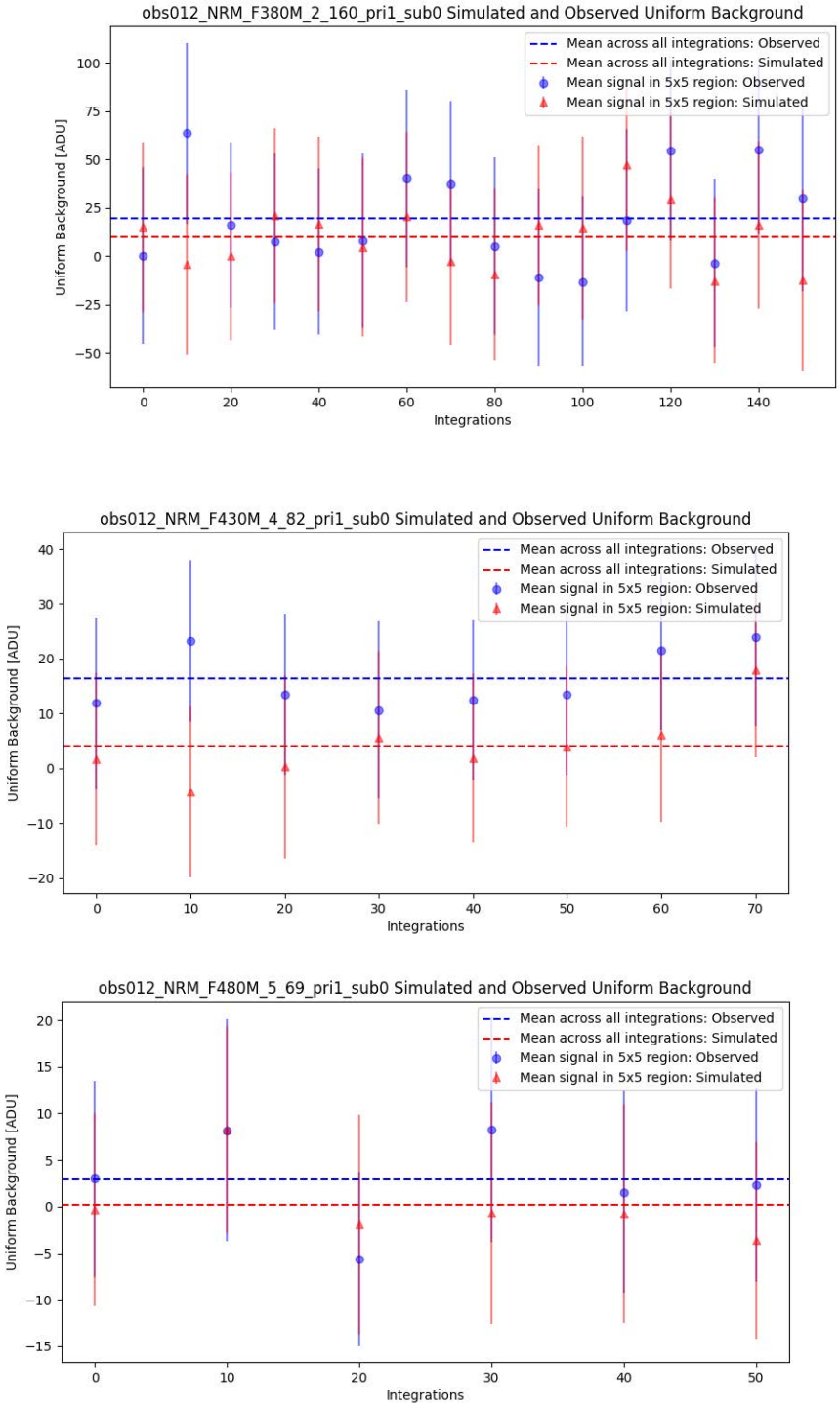

Figure 4-6. DC (pedestal) levels of detector data are stable. The simulated DC levels were slightly lower than those observed. Observed scatter of the DC level between bins of 10 integrations is consistent between simulations and observations. Typical results from all three NRM filter observations in one AB Dor AC visit are shown.

4.7 NAP step 5: Subaperture positions check

A data-derived linear 2d distortion map (2x2 matrix of constants) of actual NRM to model NRM pupil coordinates, at stated filters' central wavelengths should have the following properties: the absolute value of the transformation's determinant should be within 0.05 of unity, and the rotations of both V2 and V3 under the transformation should be < 5 degrees. This assumes the nominal pixel scale for NIRISS taken from the data file headers' 2x2 CD matrix.

The data-derived matrix determinant's absolute value is 1.0087 +/- 0.003 (satisfying the 0.05 deviation from unity requirement). Figure 4-7 shows the measured difference between the measured and expected position of each subaperture for each integration in a single exposure before and after the measured distortion correction was applied.

Data-derived rotation is 0.387 +/- 0.02 degrees, satisfying the < 5 degree requirement.

The full matrix is:
Xscale = 1.0072 +/- 0.002
Yscale = 1.0014 +/- 0.001
Xshear = -0.00619 +/0 0.0006
Yshear = 0.00732 +/- 0.0004

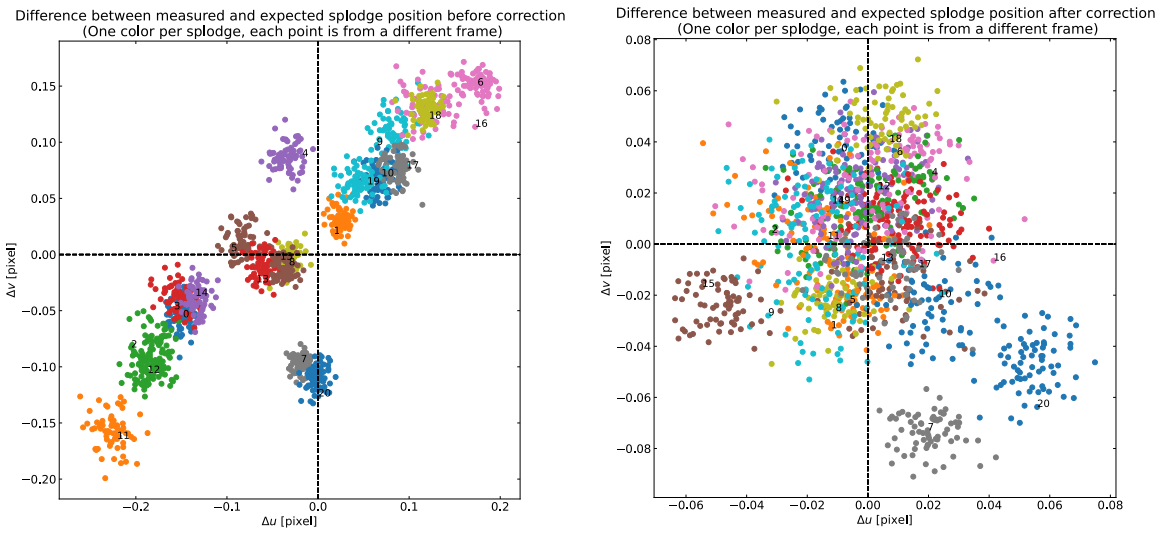

Figure 4-7. Subaperture position check. Data-derived subaperture locations (left) and offsets from expected locations (right) in uv-plane coordinates. The uv-plane is the space of baselines, measured in wavelengths (or 'cycles') of a representative wavelength. The pixel pitch in the uv-plane is the inverse of the field of view (FOV) measured in resolution elements λ/D.

4.8 NAP step 6: PSF location check

Comparison of the actual PSF location with commanded pixel location indicates successful TA. Check that measured position of all targets lie within a 0.25 pixel scalar distance of the commanded position in both axes. PSF positions were measured with a simple implementation of the Anderson & King algorithm that utilized a 21-times oversampled unaberrated NRM PSF generated with WebbPSF to match the 3 x 3 core of the PSFs. Almost all PSF positions were within 0.25 pixels of the pixel center (the nominal pixel scale is 65.6 mas/pixel). Each filter

displays systematic offsets consistent with Holfeltz et al. (2015). This supports using filter-specific offsets to place targets within 0.1 pixels of the desired location, usually the pixel center. Figure 4-8 shows the measured offsets from the commanded position (pixel center) for each integration of all primary dithered exposures. Filter-to-filter offsets from the F480M PSF position, after target acquisition, are:

Filter	X/pixels	Y/pixels
F380M	0.055	-0.221
F430M	-0.254	0.141

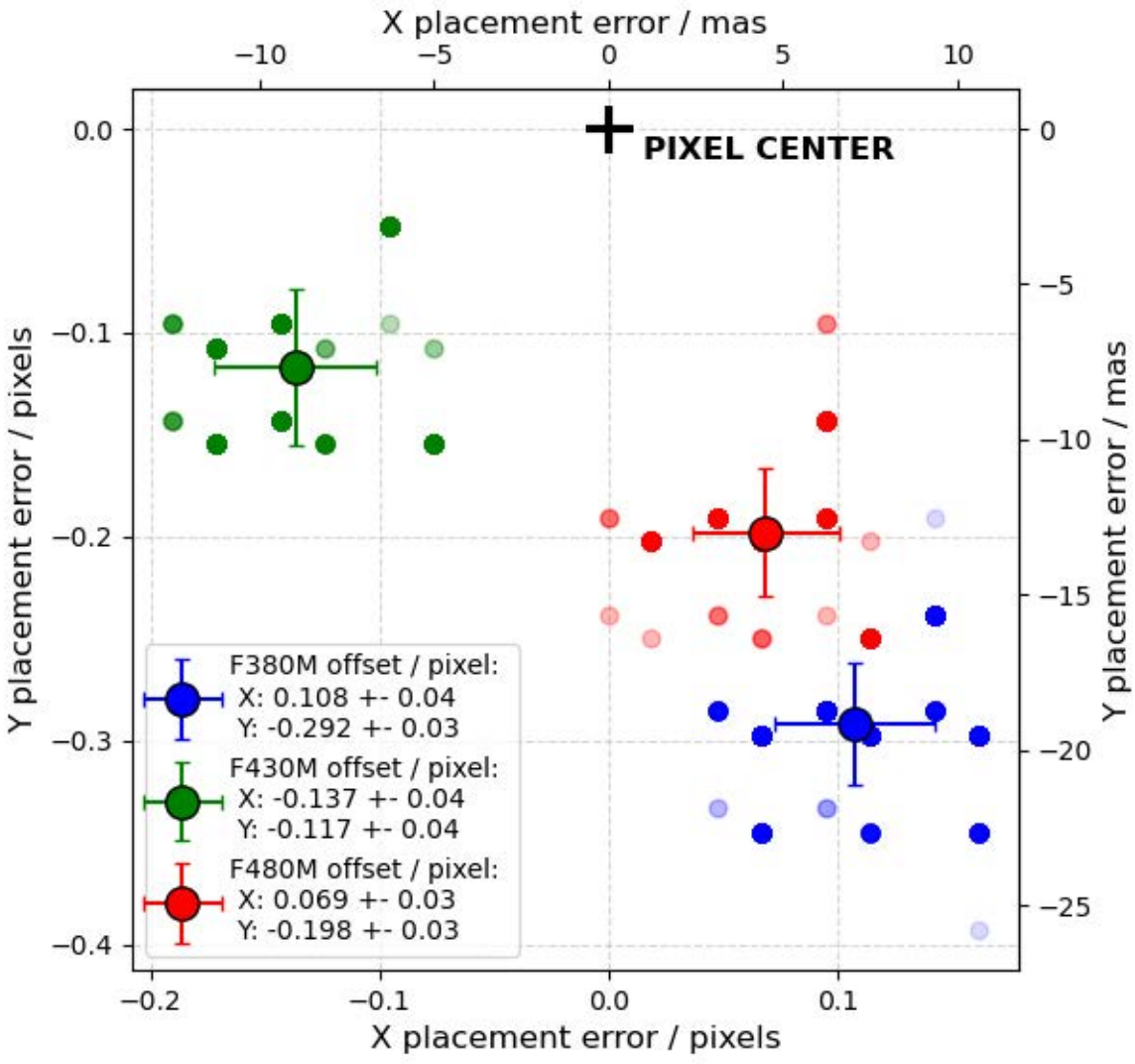

Figure 4-8. PSF locations for all TA placements to the first dither position (with and without user-defined OFFSETs) color-coded by filter. The plot shows clear filter-dependent systematic offsets from the commanded position. Positions measured using a 21x21 subpixel grid spacing with the Anderson & King (2000) algorithm are plotted with transparent markers to show repeatability of position. One-off small (~0.1 pixels) deviations show as lighter colored markers.

4.9 NAP step 7: Dithers and Subdithers location check

Dithers and sub-dithers should match the commanded values. (Measured pixel position of all targets lie within 0.25 pixel scalar distance of the commanded position in both axes. Successive sub-dither position differences should have standard deviations consistent with known SAM accuracy and commanded values).

In the re-observation of NIS-019, pri2 was treated as a direct placement rather than an offset, so we apply the same pri1 criteria to this position.

Sub-pixel dither pattern placements were measured in each integration of two 5-point and one 25-point subpixel dither patterns. The expected (commanded) position is taken from the header XOFFSET and YOFFSET keywords and transformed from the Ideal to Science coordinate frames. The position in each integration of an exposure is measured using an iterative interpolated shift method.

We find that the measured positions of each sub-pixel dither for both the 5-point and 25-point dither patterns falls well within 0.25 pixel of the commanded position (~0.016 arcsec), as can be seen in the left-hand plots of Figures 4-9 and 4-10. The scatter of the positions in individual integrations is also consistent with known measurements of the pointing stability (e.g. Rigby et al 2022.)

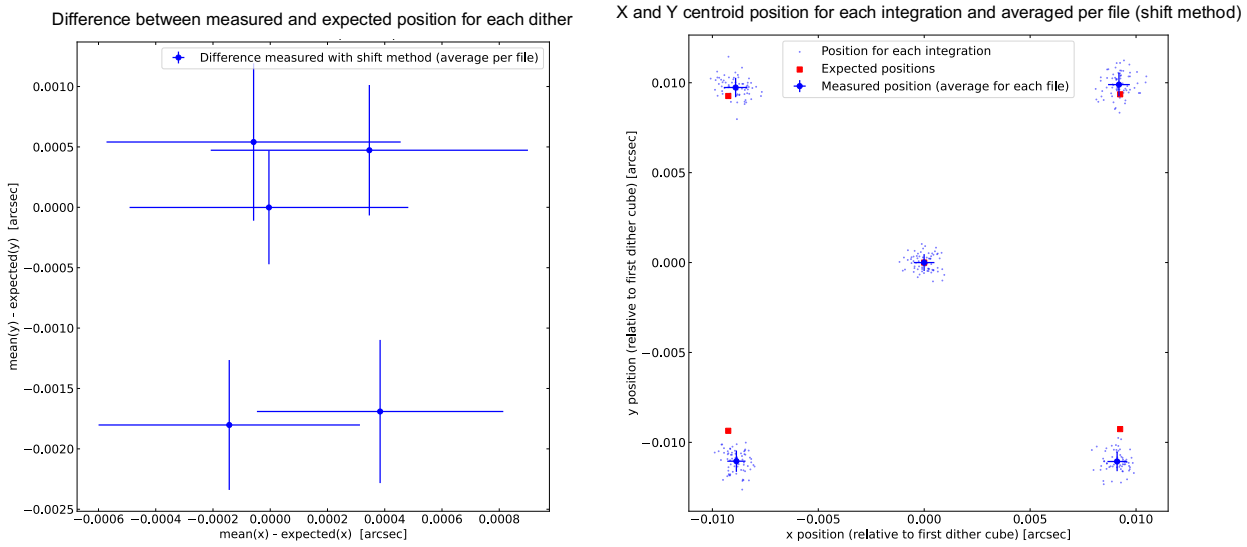

Figure 4-9. Left: Average difference between the measured and commanded PSF positions for a 5-point subpixel dither pattern, where each point is the average of multiple integrations in an exposure. Right: Centroid position relative to the first position for the same 5-point subpixel dither pattern (blue points) and the expected position (red points).

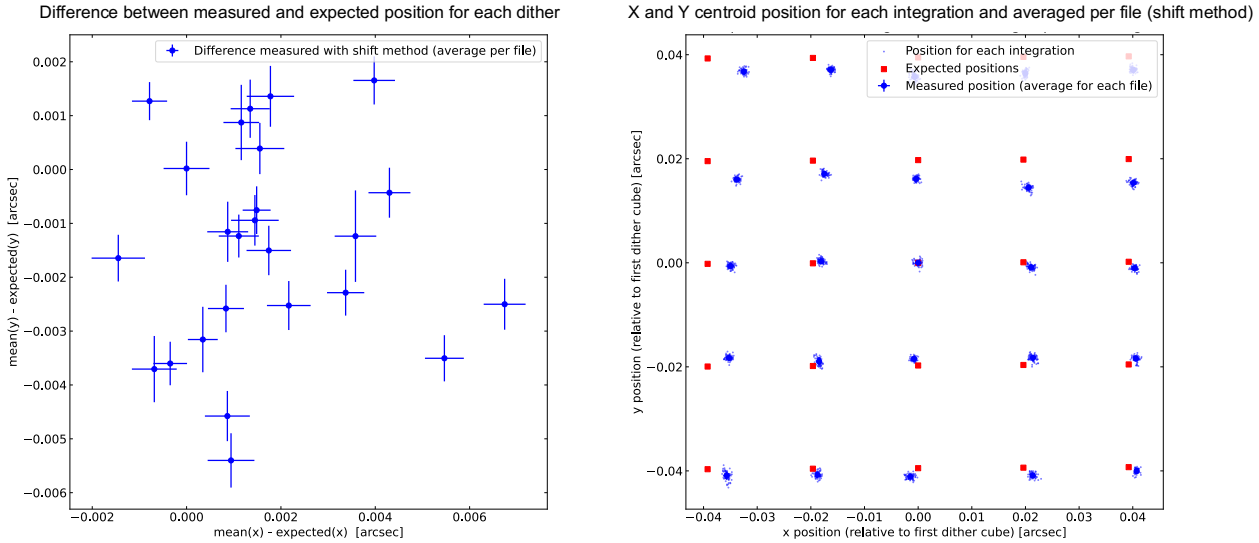

Figure 4-10. The same as above, but for a 25-point subpixel dither pattern.

4.10 NAP step 8: Charge Migration existence

Using signal limits of 30,000e- and 72,000e- data, count rates as a function of exposure in the pixel are measured. Departures of 1% from linearity are acceptable at the highest signal level.

AB Dor exposures in F480M at two detector positions were divided into “chunks” of groups -- e.g. a ramp with input shape (nint, ngrp, nrow, ncol) = (60,12,80,80) divided into four chunks will result in four files each with shape (60,3,80,80). The chunks of groups are then processed as separate exposures in the pipeline, and a stack of difference images (early groups minus each subsequent chunk of groups) constructed from the 2D cal files. The change in count rate in the peak pixel and in the surrounding 8 pixels is plotted as a function of group-chunk number for each case; a representative example from a 72,000e- peak signal exposure is shown in Figure 4-11, along with linear and quadratic fits to the data. Nonlinearity is calculated as a percent change from the starting chunk of groups. The 30,000e- data showed ~1% decrease in count rate at the highest signal level, while the 72,000e- data showed ~11% decrease (Figure 4-12). Based on these results, we do not need to revise the recommended signal limit down from 30,000 e- ahead of Cycle 1 science, nor will we raise it to 72,000 e-. Further exploration of commissioning and early Cycle 1 data should provide more insight into AMI sensitivity to charge migration and strategies for mitigation of its effects.

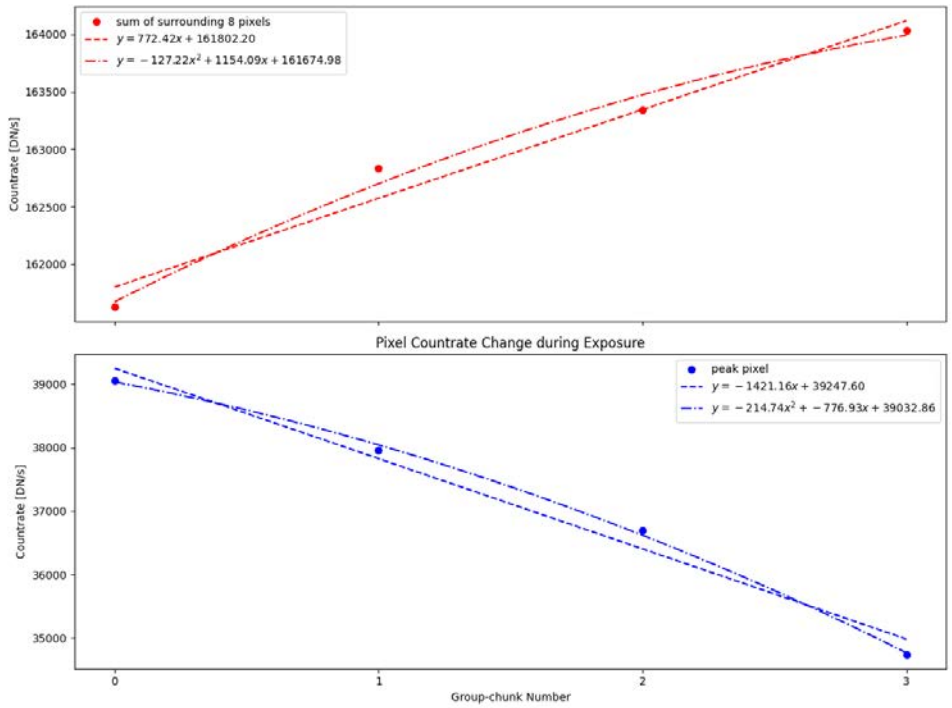

Figure 4-11. Count rate in the peak pixel (bottom pane) and in the surrounding 8 pixels (top pane) is measured as a function of signal level in four chunks of groups going up the ramp. In this case, the 72,000 e- signal limit data is split into 4 chunks of groups, and the count rate in the peak pixel is seen to decrease as the sum of the count rates in the surrounding pixels increases, indicating charge migration occurred.

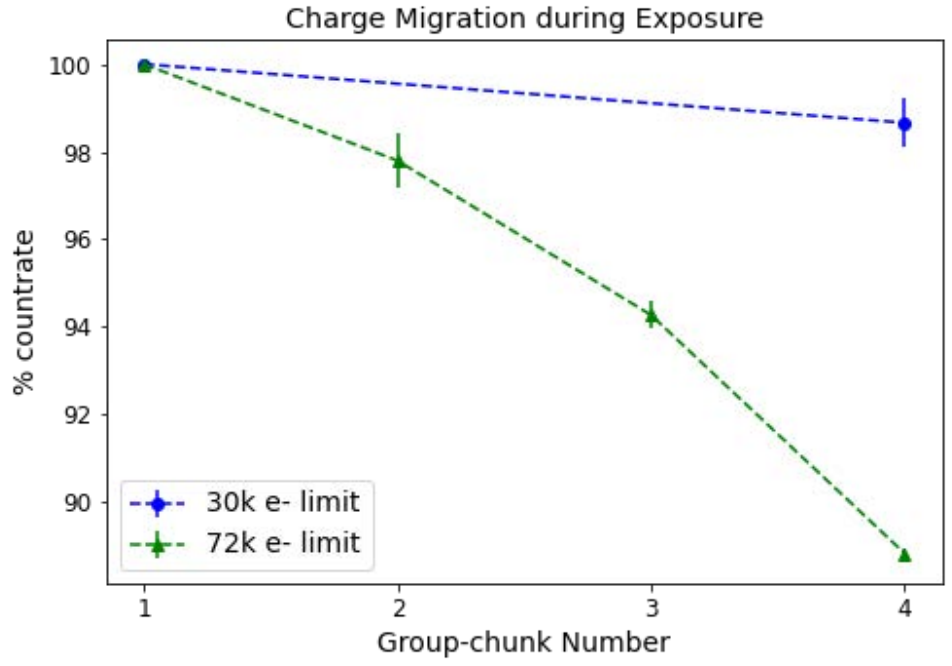

Figure 4-12. Charge migration observed in the peak pixel during 30,000 e- and 72,000 e- signal limit exposures, as percentage of the count rate in the first chunk of groups. Points are averaged from the two exposures taken at two detector positions.

4.11 NAP step 9: PSF Characterization

Reference star observations 15, 16, 18, and 19 were used to compare observed AMI PSFs to those simulated with WebbPSF. Metrics used were sharpness and central pixel fraction (CPF), where the Casertano 1995 definition of sharpness as the squared sum of the intensity in a small fixed-size box divided by the sum of the intensities squared is used. We do not measure encircled energy, due to the extent of the AMI PSF and the small size of the SUB80 array. An 11x11 pixel box around the PSF peak is used to calculate sharpness in each integration of the selected primary-dithered reference star exposures, and a 35x35 pixel box used to calculate central pixel fraction. The same quantities are also calculated from noiseless WebbPSF simulated PSFs and compared to the distribution of sharpnesses and CPFs of the observed PSFs (Figure 4-13). The small difference between the quantities measured from observed versus simulated PSFs is assumed to be attributable to noise in observed PSFs and the sub-pixel difference in PSF placement between simulation and observation.

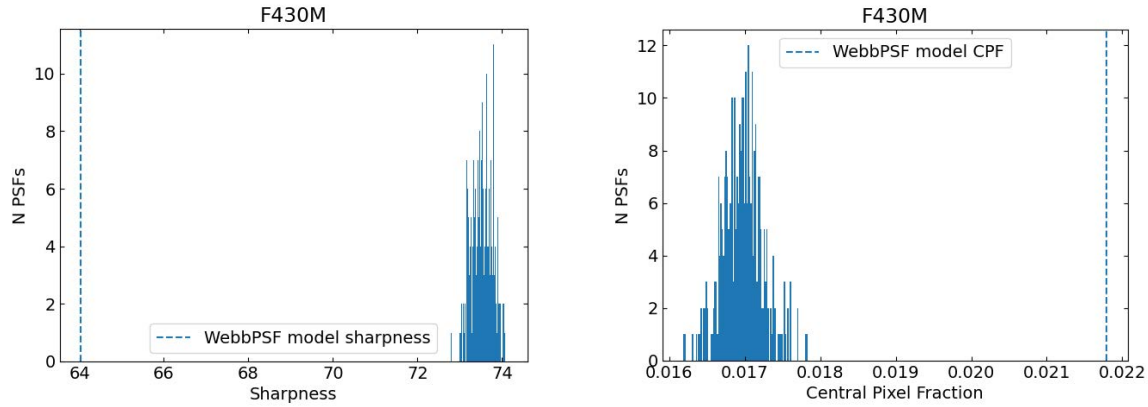

Figure 4-13. Left: Sharpness calculated in 11x11 pixel cutouts for reference star observations in the reobserved program 1093. Right: Central pixel fraction calculated in 35x35 pixel cutouts from the same PSFs.

4.12 NAP step 10: Kernel Phase Interferometry Testing

KPI analysis demonstrates recoverable contrast of at least 5 magnitudes (at 3σ) from the 2-dimensional detectability map in the KPI working range of separations. Four targets thought to be single stars were selected to demonstrate KPI with the AMI observing template. Following the first epoch of observations one target was found to be a binary, with a 1.7 dM contrast companion at 0.15 arcsec separation. When the program was reobserved, this target was omitted. After the second set of observations, another companion was found among the three remaining targets. While this companion has a slightly larger separation than the other one (0.24 arcsec), it also has a much higher contrast of ~5.6 mag, nicely demonstrating that KPI is exceeding its science readiness criterion. A representative example of the redundancy and Fourier amplitude curves and the recovered kernel phases for a single star is shown in Figure 4-14. Figure 4-15 demonstrates that AMI reaches deeper contrasts than KPI for the same number of collected photons, particularly at small angular separations. However, the much lower throughput of the NRM mask means it requires more than five times the exposure time to collect the same number of photons as the full pupil used for KPI (Kammerer et al. 2023).

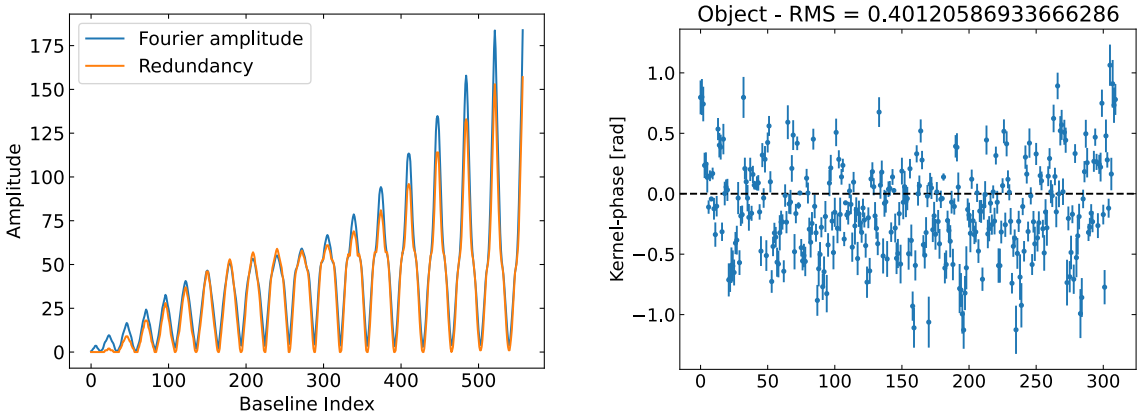

Figure 4-14. Left: Fourier amplitude and baseline redundancy are plotted against the baseline index for target J062802.01-663738.0. The agreement between the two curves plotted indicates the accuracy of the CLEARP pupil model used. Right: Kernel phases in radians are plotted against baseline index for the same target. Kernel phases for a point-like source are expected to be zero.

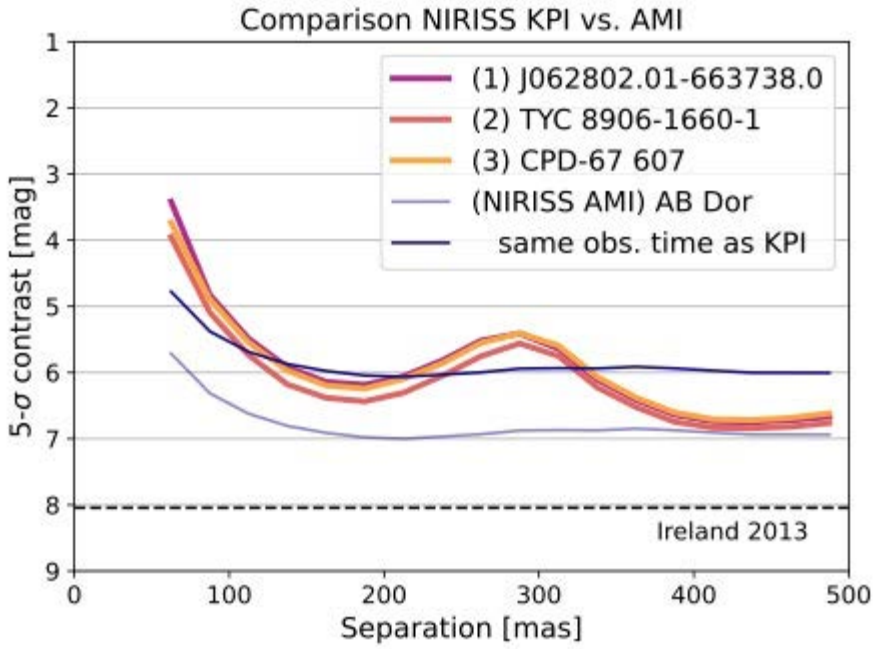

Figure 4-15. Comparison of AMI and KPI detection limits measured from NIS-019 data. Both the KPI and the AMI observations were designed to collect 2e8 photons on the detector and use the same F480M filter. The light blue curve shows the AMI detection limits extracted from the data and the dark blue curve shows the same limits after correcting them for the difference in throughput between the AMI and the KPI observations, i.e., multiplying them by $\sqrt{0.84/0.15}$, so that they correspond to the same amount of observing time. The fundamental photon noise floor for AMI according to Ireland (2013) is shown by a dashed black line. (Figure and caption used with permission from Kammerer et al. 2023)

Results

The primary purpose of this commissioning activity was to demonstrate that the AMI mode was ready for science. A summary of these results was presented at AMI Science Readiness Review held at STScI on June 14, 2022, and involved the entire JWST Project. At the review the AMI mode was declared to be ready for science.

5 References

Anderson, Jay and King, Ivan R. "Toward High-Precision Astrometry with WFPC2. I. Deriving an Accurate Point-Spread Function". *PASP* 112. 776 (2000): 1360-1382.

Casertano, Stefano. “Focus monitoring and recommendation for secondary mirror move”. Instrument Science Report, No. OTA 18. 1995.

Gallenne, A., Mérand, A., Kervella, P., Monnier, J. D., Schaefer, G. H., Baron, F., Breitfelder, J., Le Bouquin, J. B., Roettenbacher, R. M., Gieren, W., Pietrzynski, G., McAlister, H., ten Brummelaar, T., Sturmann, J., Sturmann, L., Turner, N.,Ridgway, S. and Kraus, S. “CANDID: Companion Analysis and Non-Detection in Interferometric Data”. Astrophysics Source Code Library, record ascl:1505.030 (2015)

Holfeltz, S., Goudfrooij, P., & Sivaramakrishnan, A. 2015, “NIRISS Target Acquisition Centroid Simulations”, JWST-STScI-0003963 (Baltimore: STScI)

Ireland, M.J. "Phase errors in diffraction-limited imaging: contrast limits for sparse aperture masking". *MNRAS* 433. 2(2013): 1718-1728.

Kammerer, Jens et al. "Kernel phase imaging with VLT/NACO: high-contrast detection of new candidate low-mass stellar companions at the diffraction limit". *MNRAS* 486. 1(2019): 639-654.

Kammerer, Jens et al. “The Near Infrared Imager and Slitless Spectrograph for JWST – V. Kernel Phase Imaging and Data Analysis”. *PASP* 135. 1043 (2023): 014502.

Rigby, Jane et al. “The Science Performance of JWST as Characterized in Commissioning.” To appear in *PASP* (2023), arxiv:2207.05632.

Sahlmann, Johannes. “Orbit and Masses of AB Dor A/C Revisited.” Private communication (2017).

Sivaramakrishnan, Anand et al. “The Near Infrared Imager and Slitless Spectrograph for the James Webb Space Telescope. IV. Aperture Masking Interferometry”, *PASP* 135. 1043 (2023): 01500.